Composites Part B 211 (2021) 108669

Contents lists available at ScienceDirect

Composites Part B

journal homepage: www.elsevier.com/locate/compositesb

Flexible and lightweight melamine sponge/MXene/polyborosiloxane (MSMP) hybrid structure for high-performance electromagnetic interference shielding and anti-impact safe-guarding

Min Sang [a], Yuxuan Wu [b], Shuai Liu [b], Linfeng Bai [a], Sheng Wang [b], Wanquan Jiang [a,*], Xinglong Gong [b,**], Shouhu Xuan [b,c,***]

[a] Department of Chemistry, University of Science and Technology of China (USTC), Hefei, Anhui, 230026, PR China
[b] CAS Key Laboratory of Mechanical Behavior and Design of Materials, Department of Modern Mechanics, USTC, Hefei, Anhui, 230027, PR China
[c] National Synchrotron Radiation Laboratory, University of Science and Technology of China, Hefei, Anhui, 230027, PR China

ARTICLE INFO

Keywords:
Melamine sponge (MS)
MXene
Adhesion
Anti-impacting
Electromagnetic interference (EMI) shielding

ABSTRACT

With the development of electronic devices, human beings are always disturbed by the widespread electromagnetic radiation. Meanwhile, the impact kinetic energy from external object will also cause injuries to precision electronic instrument itself and human body. Herein, a lightweight and flexible Melamine Sponge/MXene/Polyborosiloxane (MSMP) hybrid structure with both anti-impacting and electromagnetic shielding performance is proposed by incorporating conductive $Ti_3C_2T_X$ and polyborosiloxane (PBS) into porous melamine sponge (MS). The nanocomposite shows outstanding energy dissipation ability which can efficaciously degrade the external impact force due to the shear stiffening characteristic. Meanwhile, the nanocomposite presents an excellent electromagnetic interference (EMI) shielding ability with a maximum SE_T value of 39 dB. Besides, the MSMP displays obvious adhesion property after being cut due to the viscoelastic property and internal supramolecular network of PBS, thus can repeatedly resist the external damage. Finally, a safety sports protective equipment is developed by integrating the MSMP nanocomposite into the common sportswear. Owing to the good integration of safe-guarding performance and EMI shielding properties, the MSMP nanocomposites show high prospective potential in precision electronic instruments and wearable protective equipment.

1. Introduction

Nowadays, the widespread impact energy often occurs in daily life from physical exercise, car accident and bullet shooting. These collision and harsh impact will cause discomfort, injury and even death to the human beings. Therefore, it becomes an urgent issue to develop functional wearable protective equipment for human beings. Usually, both strong energy absorption ability and comfortable flexibility are important for protection armors to adapt to the live condition. In recent years, various soft smart materials with anti-impact performance have become a hot research field for the safe-guarding of human beings [1–5]. Polyborosiloxane (PBS) is a new type of intelligent material whose viscosity can increase sharply once the applied stress is beyond the critical shear rate [6–9]. Owing to the wonderful rate-dependent shear-stiffening effect, the PBS can be applied as the resilient rubber in damping buffers and shock absorption, thus exhibits broad potential in soft body armors, vibration controlling, anti-impact and safe-guarding fields [10–13]. However, it is still a challenge for most conventional PBS based body armors because their single functionality conflicts with the modern wearable devices designed for complex electronic environments.

With the rapid growth of digital and smart electronic devices, electromagnetic radiation pollution as a serious problem has caused detrimental impacts on the surrounding environment for many precision electronic instruments and human beings. At present, a series of high-performance electromagnetic shielding materials have been developed to attenuate the electromagnetic (EM) radiation [14–17]. Current

* Corresponding author.
** Corresponding author.
*** Corresponding author. CAS Key Laboratory of Mechanical Behavior and Design of Materials, Department of Modern Mechanics, USTC, Hefei, Anhui, 230027, PR China.
E-mail addresses: jiangwq@ustc.edu.cn (W. Jiang), gongxl@ustc.edu.cn (X. Gong), xuansh@ustc.edu.cn (S. Xuan).

https://doi.org/10.1016/j.compositesb.2021.108669
Received 26 November 2020; Received in revised form 6 January 2021; Accepted 27 January 2021
Available online 31 January 2021
1359-8368/

research works present that introducing highly conductive component is an effective strategy to realize higher shielding levels. Among a series of conductive materials, 2D transition metal carbides (MXenes) emerge as a rising star because of their excellent electrical conductivity, large specific surface area and typical two-dimensional lamellar structure, which show promising applications in flexible sensors [18–21], energy storage [22–25] and electromagnetic shielding fields [26–29]. Chen et al. [30] proposed transparent $Ti_3C_2T_X$ MXene-welded Ag nanowires (Ag NWs) films with electromagnetic interference (EMI) shielding performance by decorating with a $Ti_3C_2T_X$ MXene coating into Ag NWs network. The hybrid structure showed a higher EMI shielding efficiency of 49.2 dB. Although encouraging advances about high-performance EMI shielding materials have been achieved, the development of wearable and potable devices puts forward stricter requirements for lighter and more flexible EMI shielding materials [31–34]. More importantly, it was difficult for most EMI shielding materials to resist external shocks and collisions while shielding electromagnetic waves, since most EMI shielding film and aerogel possess poor mechanical properties. To ensure the normal operation of the precision electronic instruments and body protection of special employees, it is highly imperative to develop lightweight, flexible, mechanically robust and anti-impacting EMI shielding materials.

Porous structures, such as microporous polymers or carbon-based networks, are attractive in both energy absorption and EMI shielding through multiple reflection and absorption nature [35–39]. Importantly, besides the lightweight and flexible advantages, the porous structure also provides wide and free spaces for the integration of other conductive fillers and/or polymer. Gu et al. [40] prepared a 3D copper nanowires-thermally annealed graphene aerogel (CuNWs-TAGA) framework by freeze-drying. Owing to perfect 3D CuNWs-TAGA conductive and porous structures, the CuNWs-TAGA/epoxy nanocomposites exhibited a maximum EMI shielding effectiveness value of 47 dB and high electrical conductivity of 120.8 S/m. Obviously, the unique designs composed of smart soft materials and conductive porous sponge hybrid networks undoubtedly meet the required demand of sustainable development. Moreover, the shear thickening polymer strengthened polyurethane (PU) sponge also exhibited a highly energy absorption ability by combining damping performance of the porous structure and shear thickening phenomenon [41]. Besides, the external impact not only causes harm to the human beings, but also induces negative influence on the electromagnetic shielding performance of the porous materials. In this case, developing sponge-like electromagnetic shielding materials with both safeguarding and anti-impact performance becomes a feasible and competitive solution because it can simultaneously prevent electromagnetic radiation and external collision, which can effectively protect precision electronic instruments and human beings, and keep the stable performance at the same time.

Herein, a flexible Melamine Sponge/MXene/Polyborosiloxane (MSMP) hybrid structure with both electromagnetic shielding ability and safe-guarding performance is reported by integrating conductive MXene and shear stiffening PBS into the 3D porous melamine sponge (MS). The unique 3D porous structure endows hybrid nanocomposites with softness and lightweight superiorities. The as-prepared MSMP hybrid nanocomposite could availably prevent human beings from the electromagnetic radiation. More importantly, due to the shear stiffening characteristic of PBS, the hybrid nanocomposites exhibit ideal anti-impacting and energy dissipation abilities, which can decrease the impact force and prevent the external injury. Even under the external impacting, the hybrid nanocomposite still possesses ideal EMI shielding ability (24 dB). To show the perfect integration and combination of EMI shielding properties and safe-guarding performance, a wearable sports protective equipment is produced by inserting the MSMP nanocomposite into a commercially common sportswear. The as-developed MSMP nanocomposite will provide bi-protection for precision electronic instruments and human beings, which exhibits promising prospects in EMI shielding, safe-guarding and wearable equipments fields.

2. Material and methods

2.1. Materials

Dimethyl siloxane, boric acid, benzoyl peroxide (BPO), ethanol (C_2H_6O) and concentrated hydrochloric acid (HCl) were purchased from Sinopharm Chemical Reagent Co., Ltd, Shanghai, China. Ti_3AlC_2 MAX phases (400 meshe size) were bought from 11 Technology Co. Ltd, Jilin, China. Lithium fluride (LiF) was provided by Aladdin chemical Co., Ltd, China. The melamine sponge (MS) was commercially available product, China. All reagents were used without further purification and distilled water was used.

2.2. Preparation of the PBS

The PBS was prepared according to our previous report [42]. In brief, boric acid was heated at 160 °C for 2 h in an oven to prepare pyroboric acid. Then, a mixture containing 15% pyroboric acid, 81% dimethyl siloxane and a small amount of ethyl was placed in a beaker. Finally, this mixture was heated in an oven for 5 h and the product was cooled down to room temperature to obtain the polyborosiloxane.

2.3. Synthesis of the MXene nanosheets

$Ti_3C_2T_X$ MXene was mainly synthesized by etching Al layer from Ti_3AlC_2 MAX phases with LiF/HCl. Firstly, concentrated HCl was diluted with distilled water to obtain a 9 M HCl solution. Briefly, 2 g LiF was added to 40 mL 9 M HCl solution followed by stirring for 30 min until LiF was completely dissolved. Then, 2 g Ti_3AlC_2 powder was slowly added into the above solution and the reaction was constantly stirred at 35 °C for 24 h. After that, the black product was washed several times with distilled water by centrifugation at 3500 rpm for 5 min until the pH of supernatant exceeded 6. The swelled clay-like sediment was then mixed with distilled water followed by ultrasonication for 2 h. The obtained suspension was subsequently centrifuged at 3500 rpm for 1 h and the final dark green $Ti_3C_2T_X$ supernatant was collected.

2.4. Fabrication of the MSMP nanocomposites

A facile dip-drying method was applied to fabricate the MSMP nanocomposite (Fig. 1a). Firstly, the MS was immersed in the synthesized MXene solution and then dried in the vacuum oven at 50 °Cfor 10 min after each immersion to obtain Melamine Sponge/MXene (MSM). The above immersion and drying process was repeated several times to control the different contents of MXene. The mass of dipped PBS in every sample was identical. To effectively immerse PBS solution into the sponge, 10 g PBS and 0.4 g BPO curing agent were dispersed in 50 mL ethanol in a beaker to obtain PBS solution. The mass concentration of PBS solution was 0.208 mg/mL. A lower concentration was used to ensure the PBS be impregnated as evenly as possible on the sponge. Thus the content of PBS dipped into the sponge can be determined by controlling the impregnation volume of the PBS solution. Subsequently, the above solution was further dipped into the MSM and dried in the vacuum oven at 40 °C for 10 min to remove the solvent. Finally, the above modified sponge was vulcanized at 50 °C for 2 h and the MSMP nanocomposite was obtained. For simplicity, the MS with different contents of MXene and PBS were defined as the MSM_XP_Y nanocomposite, where X was the bulk density (mg/cm^3) of MXene and Y was the bulk density (g/cm^3) of PBS, respectively. For example, the $MSM_{17}P_{0.25}$ nanocomposite indicated that 17 mg/cm^3 MXene and 0.25 g/cm^3 PBS were dipped into the MS. In addition, the inserted picture in Fig. 1a is the corresponding physical products with a size of $2 \times 6 \times 0.4$ cm^3. Thus, the actual contents of MXene in $MSM_{17}P_{0.25}$, $MSM_{29}P_{0.25}$, $MSM_{36}P_{0.25}$, $MSM_{45}P_{0.25}$ and $MSM_{57}P_{0.25}$ are 81.6 mg, 139.2 mg, 172.8 mg, 216 mg and 273.6 mg, respectively. Here, the actual contents of PBS in each sample are all 1.2 g (Table S1). After

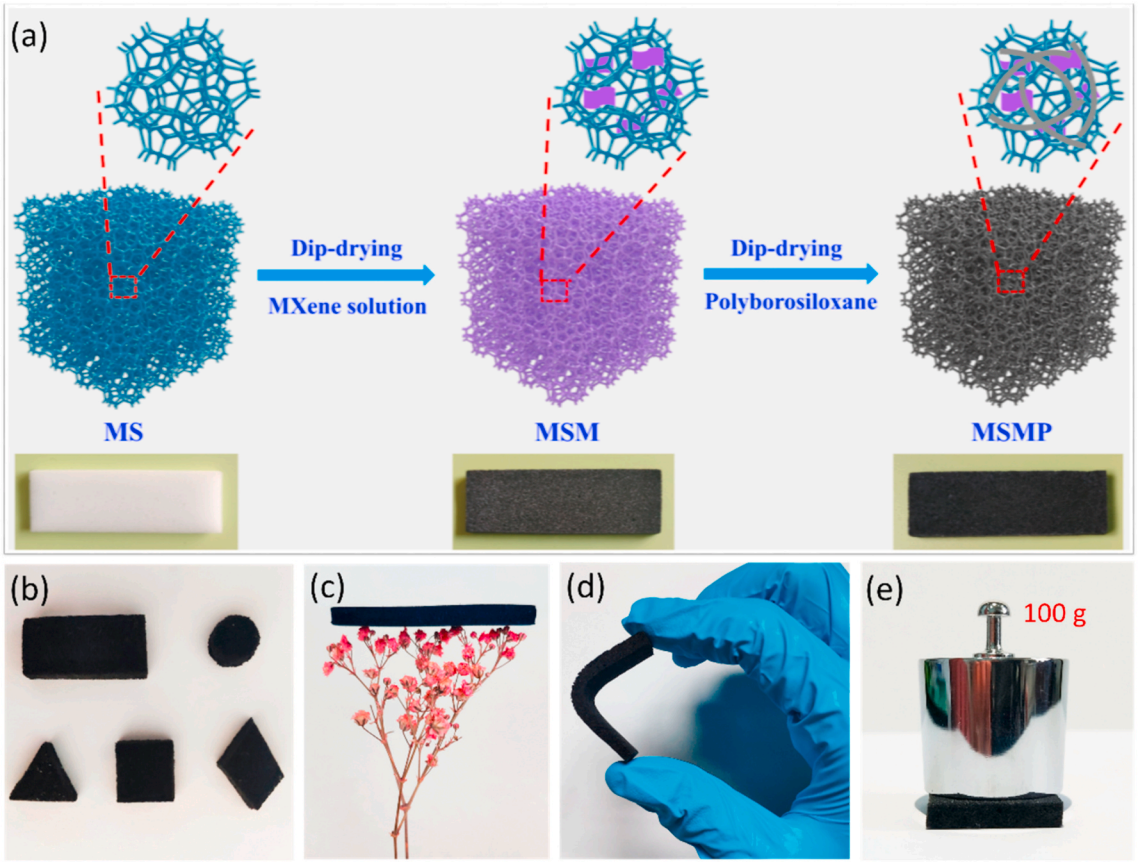

Fig. 1. Schematic illustration of preparation procedure of the MSMP hybrid structure (the inserted picture is the corresponding physical products) (a). The processable molding property (b), lightweight property (c), flexibility (d) and pressure-resistant property (e) of the MSMP material.

embedding MXene and PBS into porous sponge, the sample shows an easy molding property which can be cut into arbitrary shapes (Fig. 1b). Based on the light porous sponge skeleton, the prepared MSMP nanocomposite can be easily placed on the flower without causing any damage and deformation, presenting a lightweight advantage (Fig. 1c). Besides, the as-prepared sample possesses favorable flexibility, thus it could be bent easily (Fig. 1d). Fig. 1e shows the pressure-resistant property of MSMP material which indicates that the product can withstand the pressure of 100 g of weights without significant compression deformation.

2.5. Characterization

The surface morphologies and cross-sectional morphologies of the MXene, MS and MSMP nanocomposites were characterized by scanning electron microscopy (SEM, Sirion 200). Here, the original MSMP sample was cut by using an art knife for the cross-section characterization. Field-emission transmission electron microscopy (FETEM) images of MXene nanosheets were recorded on an FETEM JEM-2100F with an accelerating voltage of 200 kV. The height morphology of MXene nanosheets was characterized by the atomic force microscope (AFM, dimension icon, Bruker). The crystalline phase characterization of the MXene was performed by X-ray diffraction (XRD) (SmartLab, Japan). The Fourier transform infrared spectroscopy (FTIR) was tested using a Bruker alpha apparatus in ATR mode from 4000 to 650 cm^{-1} using 24 scans at a resolution of 4 cm^{-1}. The tensile properties of MS, MSM and MSMP nanocomposites were examined by the Material Test System (MTS). A commercial rheometer (Physica MCR 301, Anton Paar Co., Austria) was used to explore the shear stiffening characteristic of the PBS and MSMP specimens. Samples were molded into a cylinder shape with a thickness of 1.00 mm and a diameter of about 20 mm. The shear frequency was swept from 0.1 to 100 Hz and the strain was set at 0.1%. In this paper, a drop hammer test device was applied to study the safeguarding and anti-impacting properties of the MSMP nanocomposites. Samples were cut into small pieces with a size of $2 \times 3 \times 0.4$ cm^3. During the test, the drop hammer would fall from different heights and the force sensor installed on the bottom base could record the corresponding force signals. The electrical conductivity was measured by the standard four-point contact method on a four-point probe (FT-340, Ningbo rooko instrument Co., Ltd, China). The electromagnetic interference shielding performance of the MSMP nanocomposites was tested by ASTM D 4935-89 using a vector network analyzer (AV3672, China electronics technology instruments Co., Ltd.) in the 8–12 GHz region (X-Band). Each sample was cut into the size of 22.9×10.2 mm^2 for the test. During the test, the specimen was tightly fixed in a copper clamp and then connected between two wave-guide flanges.

3. Results and discussion

3.1. Fabrication and characterization of MXene nanosheets and PBS

Fig. 2 illustrates the synthetic procedure and characterization of MXene nanosheets. As shown in Fig. 2a, the MXene nanosheets can be synthesized *via* etching Ti_3AlC_2 precursor using LiF/HCl mixture and subsequently delaminated in deionized water by ultrasonication. After centrifugation, a stable MXene aqueous solution is finally obtained. The as-prepared MXene aqueous solution exhibits a typical Tyndall effect, which demonstrates that MXene could be well-dispersed in water (Fig. 2c). From a SEM image, the morphology of HCl/LiF-etched MXene is presented in the form of a loosely multilayer structure (Fig. 2b), which is transformed from the densely layer-stacked structure of Ti_3AlC_2 precursor (Fig. S1a). After ultrasonic exfoliation, the thin-flake structure of

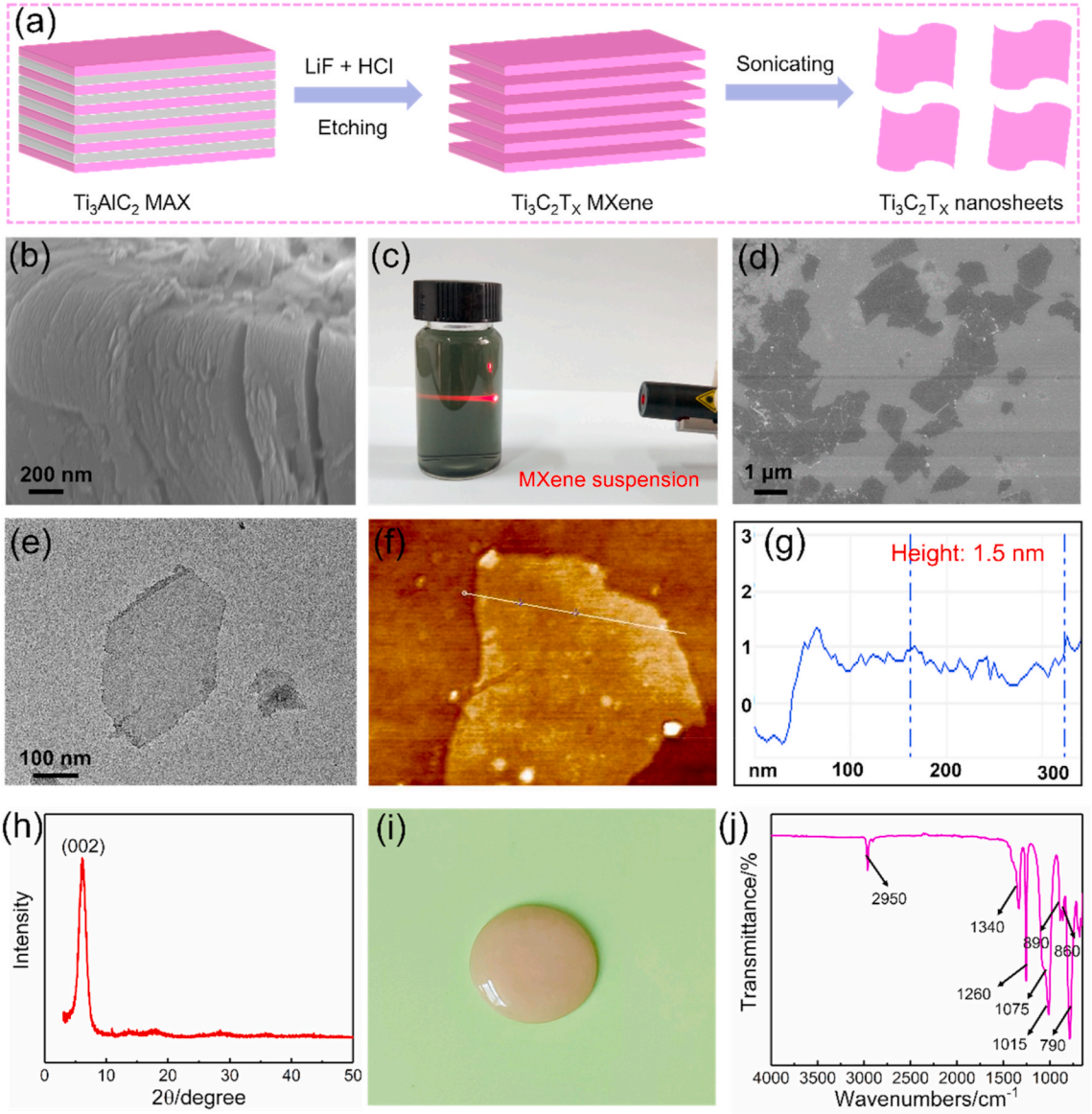

Fig. 2. Schematic illustration of synthetic procedure for $Ti_3C_2T_X$ MXene (a). SEM image of multilayered MXene (b). Photograph of the MXene aqueous solution, showing its Tyndall effect (c). SEM image (d), TEM image (e), AFM image (f), the height morphology (g) and XRD pattern (h) of the delaminated MXene nanosheets. The digital photo (i) and ATR-FTIR spectrum (j) of PBS.

delaminated MXene nanosheets can be clearly observed (Fig. 2d). TEM image also reveals the lamellate structure of MXene, confirming an obvious 2D sheet morphology with an average size of several hundred nanometers (Fig. 2e). The AFM tests also demonstrate the thickness of the MXene nanosheet is approximately 1.5 nm, further confirming the successful acquisition of single-layer MXene nanosheet (Fig. 2f and g). The crystal structures of Ti_3AlC_2 precursor and MXene are identified by XRD. From Fig. 2h, it can be seen that the characteristic diffraction peak (104) of Ti_3AlC_2 located at 39° (Fig. S1b) disappears, which proves that Al layers are completely eliminated after being etched by LiF/HCl. Meanwhile, characteristic peak (002) of the MXene shifts to a lower angle of $2\theta = 6.2°$ ($2\theta = 8.2°$ for Ti_3AlC_2 precursor), which further proves the successful synthesis of MXene nanosheets. Fig. 2i displays the digital photo of the PBS which is usually known as the silly putty. Besides, the ATR-FTIR spectrum of PBS is shown in Fig. 2j. The characteristic peaks at 2950, 1340, 1260 and 790 cm^{-1} are ascribed to $-CH_3$ asymmetric stretching, B–O vibration, Si–CH_3 asymmetric deformation and Si–C stretching vibration, respectively. Meanwhile, the peaks at 1015 and 1075 cm^{-1} derive from the stretching vibrations of Si–O–Si bond. The absorption band at 860 and 890 cm^{-1} prove the formation of Si–O–B bond [43,44].

3.2. Formation and characterization of the MSMP nanocomposites

The conductive MXene and PBS were doped into the melamine sponge (MS) in sequence *via* a simple dip-drying method. During the fabrication, scanning electron microscopy (SEM) was conducted to track the structure evolution. Fig. 3 shows the microstructures of pristine MS, MSM and MSMP nanocomposites, respectively. As shown in SEM images, the pristine MS displays an obvious three-dimensional and cellular-like porous network structure, which provides a stable and robust porous framework for the subsequent adhesion of MXene and PBS (Fig. 3a, d, g). After coating MXene, the porous network of MS is filled with visible MXene nanosheets and little sponge backbone could be clearly seen (Fig. 3b, e, h). Subsequently, the PBS is further dipped into the hybrid sponge. As shown in Fig. 3c, f, i, the PBS is tightly impregnated into the sponge scaffold and shows a cage construction, which makes the network structure of sponge could no longer be clearly

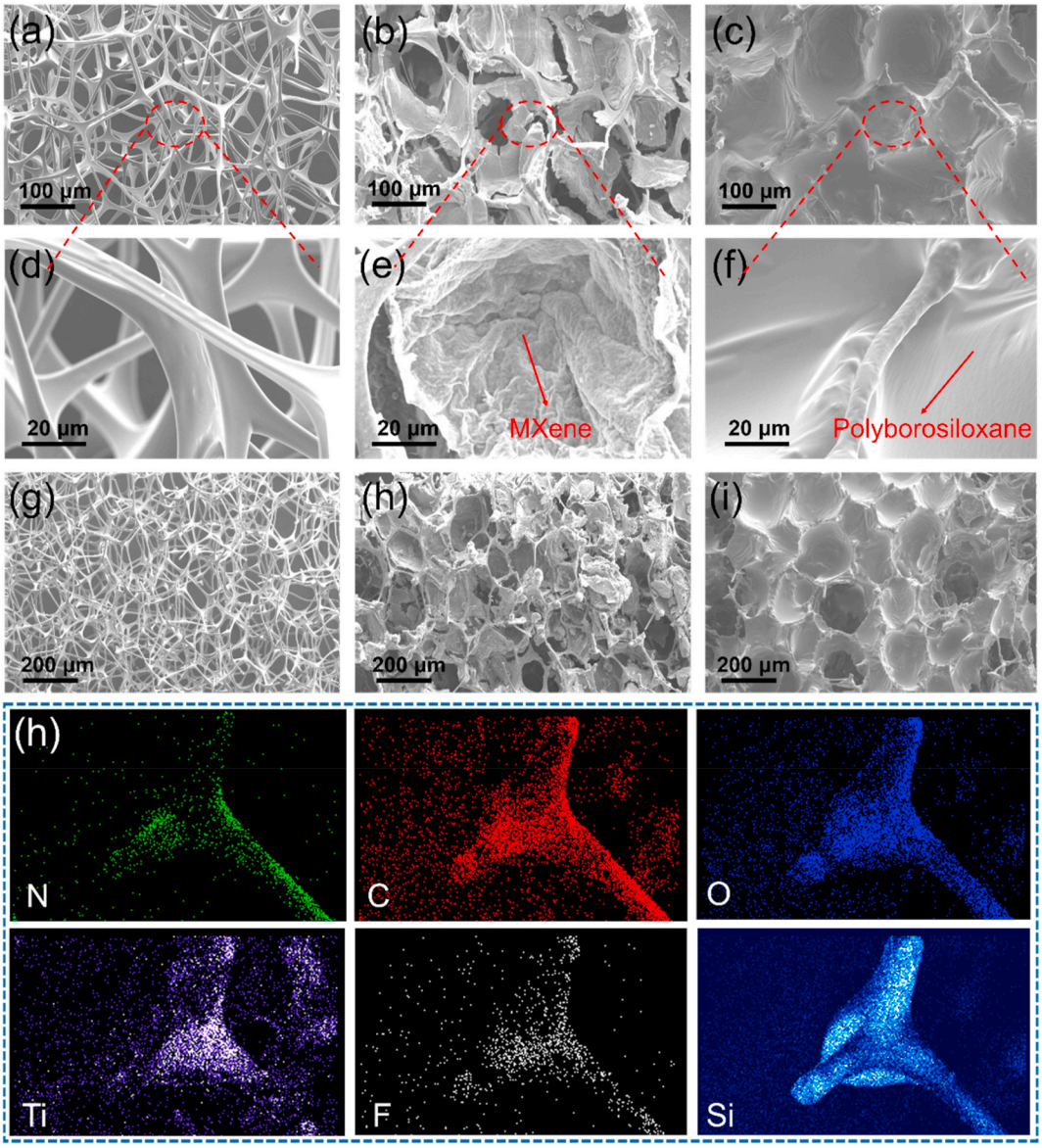

Fig. 3. SEM surface images of the pristine MS (a, d), MSM_{17} (b, e) and $MSM_{17}P_{0.25}$ nanocomposite (c, f). The corresponding SEM cross-sectional images of the pristine MS (g), MSM_{17} (h) and $MSM_{17}P_{0.25}$ nanocomposite (i). Elemental mapping images of the MSMP material (h).

observed. Additionally, the cross-sectional images (Fig. 3g, h, i) of samples show similar morphologies with surface images, indicating that the structure of original sponge is isotropous, while MXene nanosheets and PBS are uniformly filled into the melamine sponge. Fig. S2 further shows the digital image of the homogeneous cross-section of the MSMP nanocomposites. Melamine sponge is a copolymer which consists of formaldehyde-melamine-sodium bisulfite, thus there are a lot of hydrogen bonds between formaldehyde and melamine molecules. Fortunately, there are also a large number of functional groups, such as –O, –F and –OH, on the surface of MXene nanosheets. Therefore, the interfacial hydrogen bonds formed between MS and MXene nanosheets promote the well interaction between MXene and MS. Besides, the porous structure of MS also provides a broad free space for the self-accumulation of MXene nanosheets. After further impregnating PBS, the electron-rich O atoms in PBS molecules can also share electrons with H atoms on the surface of MXene nanosheets *via* hydrogen bonds to form a strong interfacial interaction. More importantly, the PBS is viscoelastic and the surface is sticky, thus it can well adhere on the MSM *via* a facile dip-drying approach. Therefore, it is proven that the dip-drying method is effective to obtain the final MSMP nanocomposites with homogeneous dispersion of MXene nanosheets and PBS matrix in 3D melamine sponge.

Elemental mapping was employed to investigate the elemental distributions and compositions of MSMP nanocomposite. Melamine sponge is a copolymer which consists of formaldehyde-melamine-sodium bisulfite [45–47]. The pristine sponge mainly contains C and N elements. From the distribution of C and N elements, an obvious 3D skeleton structure could be clearly observed (Fig. S3). After doping MXene, the elemental mapping images and EDS spectrum of MSM in Fig. S4 prove the coexistence of Ti, O and F elements. Moreover, Ti element is distributed through the entire structure, indicating that MXene nanosheets are successfully penetrated into the porous sponge network. For MSMP nanocomposite, the elemental mapping images suggest a new signal of Si element which is originated from the polyborosiloxane, further confirming the good combination of PBS with MSM nanocomposite (Fig. 3h). Besides, the backbone of sponge could be seen by the distribution of C, O, N, Ti, F and Si elements. Based on the above elemental mapping results, the MSMP nanocomposite with a 3D network structure is finally constructed, which is consistent with the SEM analysis.

3.3. Mechanical and adhesion properties of the MSMP nanocomposites

Tensile tests are conducted to explore the mechanical property of MSMP nanocomposites by using MTS. For MS, MSM and MSMP samples, they all only go through plastic deformation before being fractured. The maximum tensile strength of MS, MSM and MSMP samples are 56, 87 and 99 KPa, respectively. Thus, the incorporation of MXene and PBS into melamine sponge finally improves the mechanical strength of MSMP composite. To explore the rheological property of MSMP nanocomposites, a commercial rheometer is used to measure the storage modulus (G′) and loss modulus (G″) at different frequencies. When the shear frequency increases, the shear rate loading on the sample also increases. As shown in Fig. 4b, with increasing of the shear frequency, the G′ of melamine sponge and MSM are basically unchanged. Owing to the shear stiffening nature of PBS (the G′ increases from 246 Pa to 0.3 MPa, Fig. S5a), the MSMP also exhibits similar shear stiffening behavior with the G′ increasing from 0.15 MPa to 0.5 MPa when the shear frequency improves from 0.1 to 100 Hz. Fig. 4c shows the loss modulus (G″) of MS and MSM, in which it decreases with the increase of shear frequency. For PBS and MSMP, the G″ experiences a increase-saturation-decrease process, which must be attributed to the energy absorption property of the incorporated PBS (Fig. S5b). As a result, the MSMP is expected to exhibit safeguarding and anti-impact functions due to the shear stiffening and energy absorption properties.

More importantly, the adhesion properties of the as-fabricated MSMP nanocomposites were explored (Fig. 4). For visual presentation of adhesion behaviors, an intact MSMP sample was firstly cut into two pieces by a knife and the two separated pieces were then contacted with each other by slight pressing. Finally, two separated pieces instantaneously stuck together after being touched, which showed an obvious adhesion properties. Similarly, another MSMP sample which was cut into four pieces also displayed excellent adhesion performance at room temperature (Fig. 4d). Since the PBS is viscoelastic at room temperature and the surface is sticky, the viscous PBS on the sponge backbone can still adhere robustly together after being severely damaged. More importantly, the formation of supramolecular networks also contributes to adhesion behavior [48]. Hydrogen bonds or coordination bonds have multiple adhesion capabilities, which can be used for the self-assembly of polymeric materials. The PBS matrix used in this work has three chemical formulas as shown in Fig. 4e. When B atoms are introduced into polydimethylsiloxane, electron-rich O atoms share electrons with electron-deficient B atoms and thus the "B–O coordination bonds" are formed. This "B–O coordination bond" is similar to the hydrogen bond, which is transient, dynamically variable and more vulnerable than covalent bond. Additionally, the electron-rich O atoms in PBS matrix also could share electrons with H atoms to form hydrogen bonds (Fig. 4e). Therefore, hydrogen bonds and B–O coordination bonds formed in PBS matrix on the sponge skeleton endow MSMP nanocomposite with ideal adhesion property. Besides, the tensile strength of MSMP nanocomposite after cutting and adhesion was also examined. The MSMP nanocomposite after cutting and adhesion also only goes through plastic deformation before being fractured and the maximum tensile strength is 3.3 KPa (Fig. S6a). Compared to the original MSMP nanocomposite (99 KPa), the tensile strength after cutting and adhesion is greatly

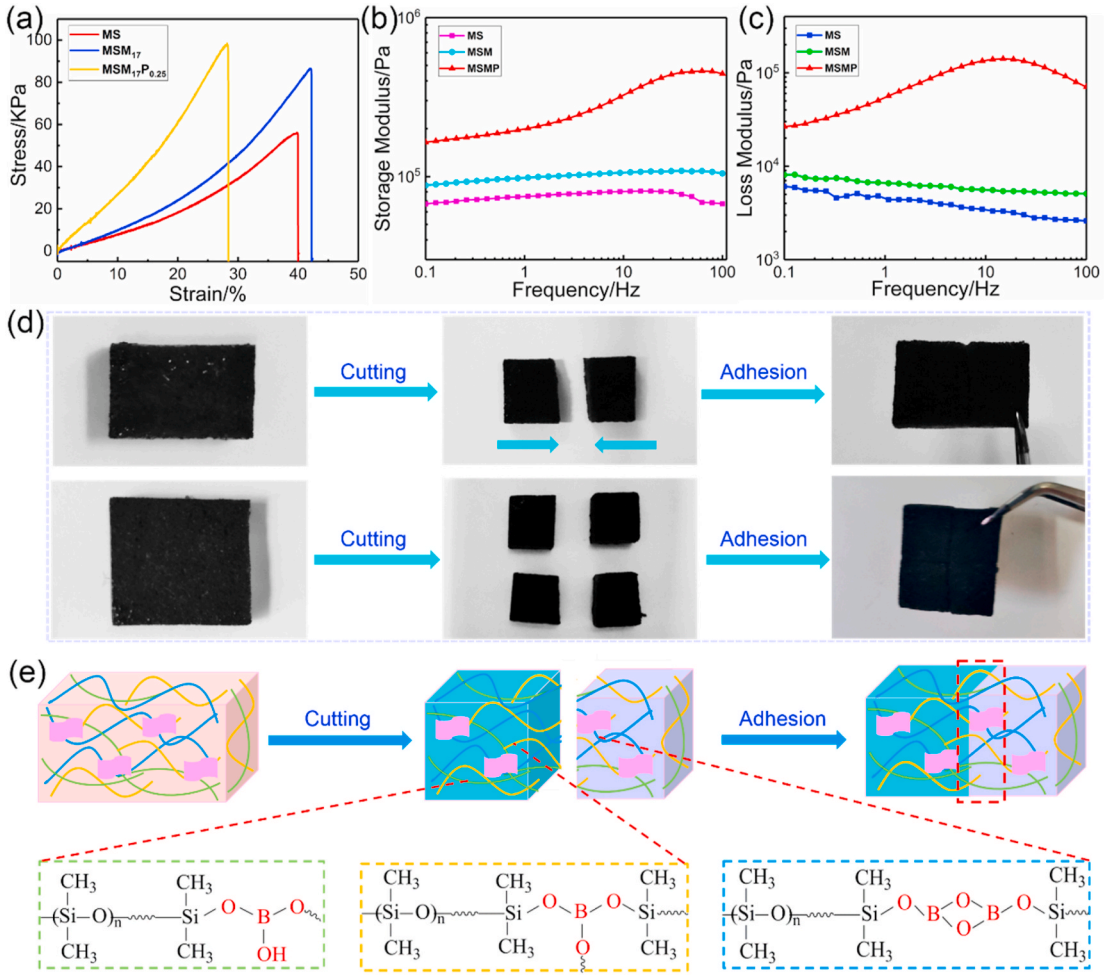

Fig. 4. The tensile stress-strain curves (a), storage modulus (b) and loss modulus (c) of MS, MSM and MSMP nanocomposites at different frequencies. Photographs (d) and schematic diagram (e) (inset is the chemical formula of PBS) of the adhesion behavior of MSMP nanocomposite at room temperature.

reduced (Fig. S6b). Importantly, the MSM nanocomposite can hardly show adhesion property and the adhesion property of MSMP nanocomposite is derived from the viscous PBS. To keep the EMI shielding performance, the content of PBS is relatively low, thus the tensile strength after cutting and adhesion is much lower than that of the original MSMP nanocomposite. However, MSMP nanocomposite still exhibits obvious adhesion property compared to the MS and MSM samples. In conclusion, the as-fabricated MSMP possesses prominent adhesion capability which can effectively prevent external damage, such as cutting and severing.

3.4. Safeguarding and anti-impact performance of the MSMP nanocomposites

To systematically investigate the safeguarding and anti-impact performance of MSMP material, a drop hammer test device (Fig. 5a and b) equipped with the force sensor and oscilloscope (Fig. 5c) was employed. During the impact, the impact forces were captured by the force sensor and then recorded by the oscilloscope. The weight of drop hammer is 0.33 kg and the drop height varies from 10 cm to 30 cm. The sample of $MSM_{17}P$ with a size of $2 \times 3 \times 0.4\ cm^3$ is fixed on the force sensor, which is further installed on a metal pedestal. In consideration of the shear stiffening property of polyborosiloxane, the impact energy dissipation behavior of $MSM_{17}P$ material with different PBS content is firstly explored. As displayed in Fig. 5d, the maximum impact force shows a

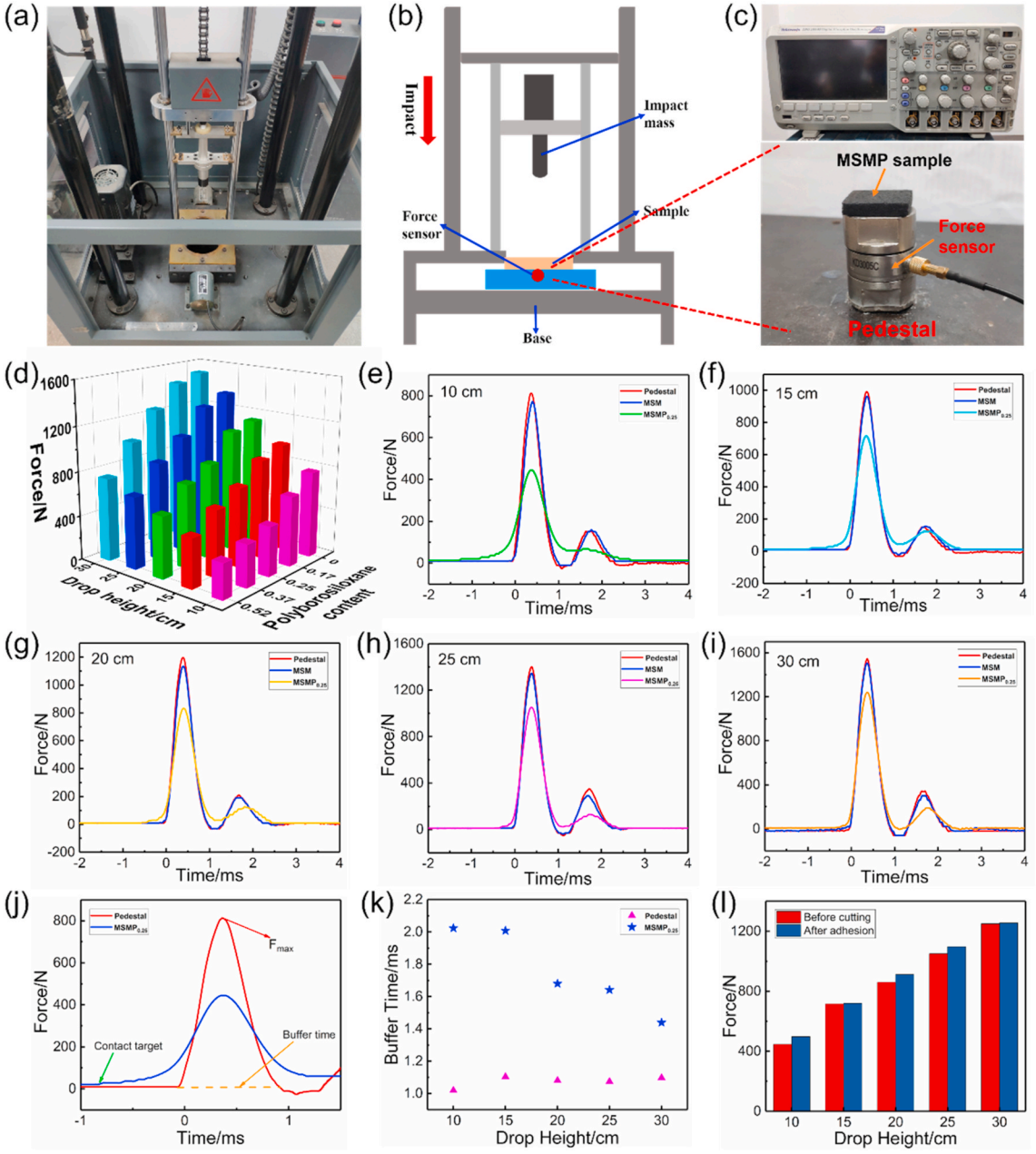

Fig. 5. The digital photo (a, c) and the schematic diagram (b) of drop hammer test equipment. Impact energy dissipation behavior of $MSM_{17}P$ material with different PBS content from 10 to 30 cm drop height (d). Typical force-time curves of pedestal, MSM_{17} and $MSM_{17}P_{0.25}$ recorded by the force transducer from drop height of 10 cm (e), 15 cm (f), 20 cm (g), 25 cm (h) and 30 cm (i), respectively (weight of the drop hammer is 0.33 kg). The comparison of buffer time between pedestal and $MSM_{17}P_{0.25}$ material (j, k). The comparison of impact energy dissipation behavior for $MSM_{17}P_{0.25}$ material before cutting and after adhesion (l).

downward trend as the content of PBS increases, demonstrating that $MSM_{17}P$ nanocomposite with higher PBS content dissipates more impact energy. Moreover, the typical force-time curves of $MSM_{17}P$ material with various PBS contents are exhibited in Fig. S7.

Herein, to detailedly describe the anti-impact performance of $MSM_{17}P$ material, the force response to drop hammer impact of pedestal, MSM_{17} and $MSM_{17}P_{0.25}$ material from 10 to 30 cm drop height are presented in Fig. 5e–i. Once the drop hammer impacts the force sensor (without sample), the impact force absorbed by the metal pedestal abruptly increases to a maximum value and then decreases to 0 in a short time. After placing sample on the force sensor, the maximum force is significantly decreased, which suggests most of the impact energy is absorbed by $MSM_{17}P_{0.25}$ material. The maximum impact force could be decreased from 817, 996, 1200, 1410 and 1550 N to 446, 716, 860, 1050 and 1250 N for 10, 15, 20, 25 and 30 cm drop height, respectively, indicating an obvious impact energy dissipation ability of as-prepared $MSM_{17}P_{0.25}$ material. It is worth mentioning that the second force peak in Fig. 5e–i is caused by the rebound after drop hammer contacted the sample. As a comparison, MSM_{17} nanocomposite without PBS is also tested, and the maximum force is just decreased a little, manifesting that the safe-guarding and anti-impact properties of $MSM_{17}P_{0.25}$ material mainly depends on the PBS. Furthermore, the impact forces of $MSM_{17}P_{0.25}$ sample with/without BPO vulcanizing agent are almost same, indicating that BPO vulcanizing agent shows slight effect on anti-impacting performance (Fig. S8). Besides, the buffer times of $MSM_{17}P_{0.25}$ material are always longer than the metal pedestal, which also demonstrates $MSM_{17}P_{0.25}$ material could effectively resist the impact and prevent external injures (Fig. 5j and k).

To further understand the stability and robustness of impact energy dissipation ability for $MSM_{17}P_{0.25}$ material, the impact force after cutting and adhesion is also measured. As shown in Fig. 5l, it could be observed that the impact force only improves a little after cutting and adhesion, which still exhibits considerable impact energy absorption ability. Therefore, the reported $MSM_{17}P_{0.25}$ material shows apparent anti-impact performance under impact condition, and the adhesion property guarantees the stability and sturdiness of performance, which highly extends the scope of applications in safe-guarding fields.

3.5. *Electromagnetic interference (EMI) shielding performance of the MSMP nanocomposite*

Essentially, high electrical conductivity of materials plays a vital role in EMI shielding ability. Fig. S9 shows the electrical conductivities of MSM nanocomposite with different MXene contents. After impregnating conductive MXene into melaming sponge (MS), the electrical conductivities of MSM_{17}, MSM_{29}, MSM_{36}, MSM_{45} and MSM_{57} samples reach to 30 S/m, 53 S/m, 98 S/m, 130 S/m and 177 S/m, respectively, which insures the high EMI performance of MSMP nanocomposite. To assess the EMI shielding ability of $MSMP_{0.25}$ composite, the EMI SE values in the X-band frequency range were tested (Fig. 6). EMI SE (SE_T) is a

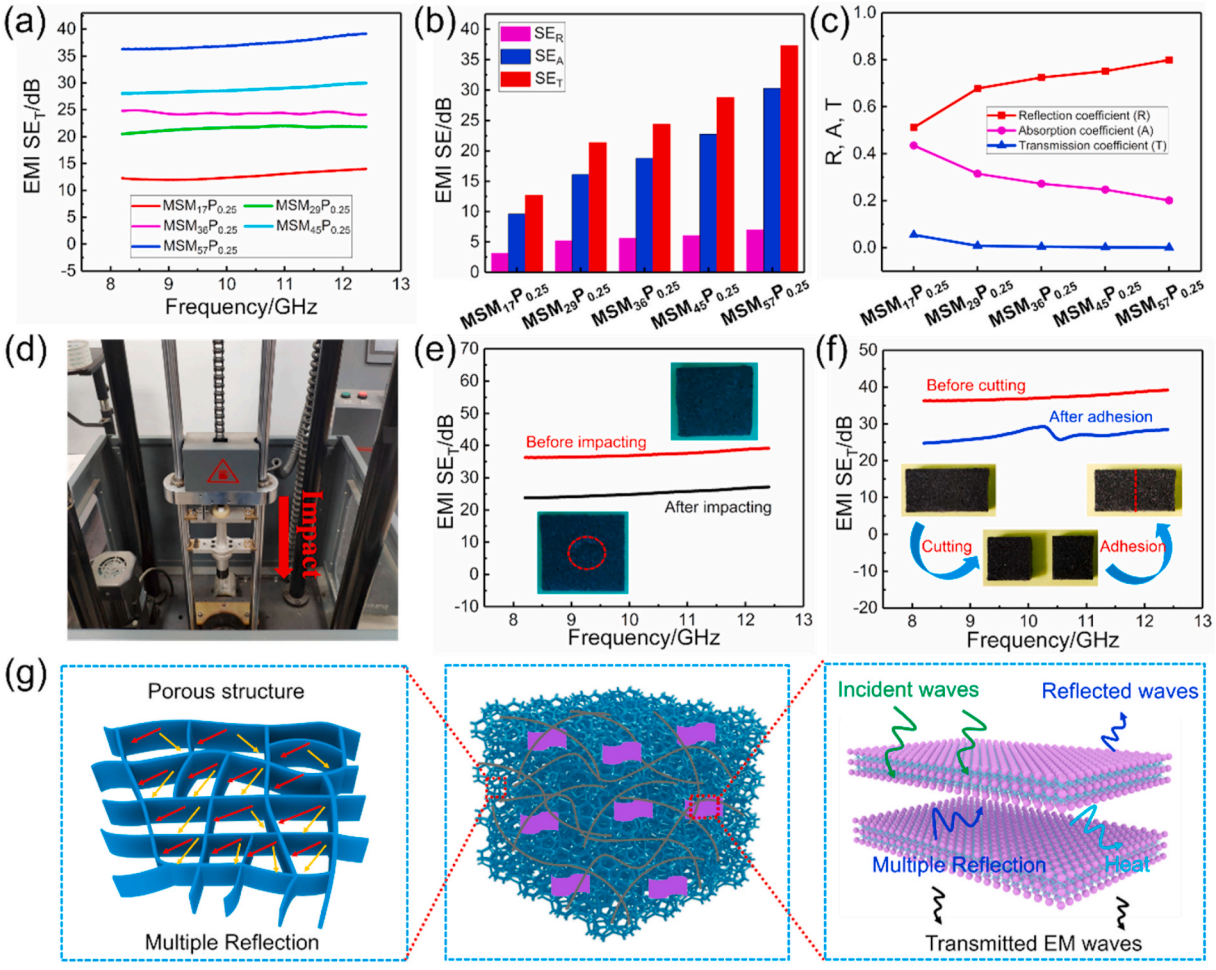

Fig. 6. EMI SE_T (a), SE_T, SE_A, SE_R values (b) and R, A, T coefficients (c) of $MSMP_{0.25}$ nanocomposite with different MXene contents. The impacting test device using a drop hammer (d) and EMI SE_T variation of $MSM_{57}P_{0.25}$ nanocomposite before and after impacting (e). The inset pictures show the initial state and impact state of sample. EMI SE_T values of $MSM_{57}P_{0.25}$ nanocomposite before cutting and after adhesion (f). The inset pictures show the cutting state and adhesion state of sample. Schematic diagram of EMI shielding mechanism of MSMP nanocomposite (g).

combination of shielding by absorption (SE_A), reflection (SE_R) and multiple reflections (SE_M) [49–51]. Usually, the multiple reflections can be neglected when the shielding thickness is larger than the skin depth. Thus, the EMI SE can be expressed as:

$$SE_T = SE_A + SE_R \quad (1)$$

The values of SE_T, SE_A and SE_R are estimated based on the S parameters measured by the vector network analyzer as follows:

$$R = 10^{\binom{S}{11}/10} \quad (2)$$

$$T = 10^{\binom{S}{21}/10} \quad (3)$$

$$A = 1 - R - T \quad (4)$$

$$SE_R = -10 \log (1-R) \quad (5)$$

$$SE_A = -10 \log (T/(1-R)) \quad (6)$$

$$SE_T = SE_R + SE_A = -10 \log T \quad (7)$$

where R is reflection coefficient, T is transmission coefficient and A is absorption coefficient.

Based on the drop hammer test, the safe-guarding and anti-impact performance of MSMP is improved with increasing the content of polyborosiloxane. However, the existence of PBS shows a negative effect on the EMI shielding ability. With increasing of the PBS content, the EMI SE_T values display a downward trend (Fig. S10). In order to balance the safe-guarding and EMI shielding performance, the optimal content of PBS incorporated into MSM is finally set as 0.25 g/cm^3. Fig. 6a shows the effect of MXene content on the EMI shielding performance. It can be seen the EMI SE_T values increase with increasing of the MXene content, and the maximum shielding value can reach up to 39 dB for $MSM_{57}P_{0.25}$ sample. In the $MSMP_{0.25}$ nanocomposite, the higher the content of conductive MXene, the more effective conductive paths (ECPs) are formed, thus leading to a higher EMI shielding performance. Furthermore, the specific EMI shielding effectiveness (SSE, SE per unit density) is an important parameter for evaluating the shielding performance of the lightweight materials. As shown in Fig. S11a, the density of $MSMP_{0.25}$ nanocomposite increases with increasing of MXene contents and the maximum density is 0.3169 g/cm^3. Because of the addition of PBS polymer, its relatively large density leads to an unsatisfactory SSE value. The average SSE value of $MSM_{57}P_{0.25}$ is 118 dB cm^3 g^{-1} (Fig. S11b). Fig. 6b exhibits the SE_T, SE_R, and SE_A values of $MSMP_{0.25}$ with various MXene contents. It is obvious that both SE_T and SE_A values increase with increasing of MXene contents, while SE_R increases slightly. Therefore, the increased EMI SE_T is mainly determined on the improved absorption rather than reflection of EM waves. To ensure the EMI shielding mechanism of MSMP nanocomposite, R, A and T coefficients are concluded in Fig. 6c. It can be seen that the R increases with increasing of MXene contents, while the A decreases. In addition, the low value of T indicates that almost incident electromagnetic waves are shielded by the MSMP nanocomposite. More importantly, the R is always higher than A regardless of MXene contents, demonstrating that the high decisive shielding mechanism is originated from reflection rather than absorption.

To verify the reliability and robustness of $MSM_{57}P_{0.25}$ material, the EMI shielding property before and after impacting and cutting is explored. As shown in Fig. 6e, the EMI SE_T value of $MSM_{57}P_{0.25}$ material decreases from 39 dB to 24 dB after impacting by a heavy drop hammer. This value is still above 20 dB thus the product exhibits a reliable EMI shielding ability. Additionally, the shielding performance of MSMP nanocomposite under the beating by the small hammerhead (175 g) is tested (Fig. S12). After 50 times of striking, the SE_T value of $MSM_{57}P_{0.25}$ nanocomposite decreases to 28 dB, which further indicates our product has a considerable excellent EMI shielding performance. More importantly, the mechanical properties and SE_T values of $MSM_{57}P_{0.25}$ nanocomposite under cycled bending, twisting and folding are exhibited in Fig. S13, further confirming the stability and reliability of EMI shielding performance in wearable device and protection of human joints. Fig. 6f displays EMI SE_T values of the MSMP nanocomposite after cutting and adhesion process. The sample is cut into two small pieces and then contacts each other to heal at room temperature for several minutes. Since the incorporation of PBS endows $MSM_{57}P_{0.25}$ material with considerable adhesion property, the EMI SE_T value (27 dB) decreases a little after cutting and adhesion, indicating a high durability of shielding performance with about 71% EMI SE retention.

Fig. 6g illustrates the EMI shielding mechanism of the MSMP nanocomposite [52,53]. Due to the impregnation of conductive MXene and the impedance mismatch of MSMP-air surface, some portions of incident electromagnetic waves are firstly reflected when contacts the surface of MSMP nanocomposite. Then remaining electromagnetic waves enter the interior of MSMP nanocomposite, and the electromagnetic radiation is absorbed through the interaction of electric dipoles in the conductive MXene nanosheets with incident electromagnetic waves, and electromagnetic radiation is transformed into other energy, like heat. In addition, the space between the adjacent MXene nanosheets and the porous structure of the sponge makes it difficult for electromagnetic waves to escape from the cage until they are attenuated and dissipated, thus achieving multiple reflections and absorption of electromagnetic waves. To further investigate the influence of porous structure on EMI shielding performance, the EMI shielding performance of $M_{17}P_{0.25}$ sample (the mixture of MXene and PBS) without the melamine sponge (MS) skeleton was tested. As shown in Fig. S14, the EMI SE_T value of $M_{17}P_{0.25}$ sample is far smaller than $MSM_{17}P_{0.25}$ sample, indicating the positive effect of porous skeleton structure on EMI shielding performance. The positive effect can be explained by two reasons: (1) the porous skeleton structure provides a wide space for the adhesion of MXene, which is conducive to form the continuous and effective conductive network; (2) the porous structure can contribute to the electromagnetic waves absorption *via* enhancing the multiple scattering in the sponge. Here, the EMI shielding performance of other previously reported nanocomposites are consulted in Table S2. It is found that the $MSM_{57}P_{0.25}$ nanocomposite shows an excellent EMI shielding ability [54–60]. In conclusion, the $MSMP_{0.25}$ nanocomposites possess ideal EMI shielding function with high cycling stability, thus they would be widely applied in protecting military device or human beings from electromagnetic radiation.

3.6. MSMP safety clothing for sports protective equipment

With the improvement of living standard, more and more people try to keep healthy by taking a variety of exercise, such as boxing, running and weightlifting (Fig. 7e). However, the athletes will inevitably be subjected to some accidental injuries during the exercise, such as abrasions, collisions, electromagnetic radiation in many special environment and so on. In order to effectively prevent external hurts and protect the sportsmen, a kind of safety protective clothing is developed by embedding the prepared $MSM_{57}P_{0.25}$ into the common sportswear. As shown in Fig. 7a, the $MSM_{57}P_{0.25}$ material can be used as a liner to fit well with the ordinary sportswear. To make it firmly and tightly embedded in the sportswear, thin gauze is used to wrap it. Finally, a safety sportswear with $MSM_{57}P_{0.25}$ protective liner is successfully obtained. Usually, sportsmen will be accidently collided by different objects during the exercise. Thus, to investigate the protective performance of the obtained safety clothing, the force under the impact of objects with different mass are tested. Compared to the common sportswear, the impact force of $MSM_{57}P_{0.25}$ safety clothing is significantly reduced from 1950 and 810 N to 1130 and 436 N when impacted by 0.33 kg and 0.54 kg objects (Fig. 7f and g) from 10 cm drop height, indicating that $MSM_{57}P_{0.25}$ safety clothing possesses obvious protective ability, which can resist the different collisions, so as to safeguard the sportsmen. More importantly, the as-prepared MSMP material displays a human compatibility and can be attached to different body parts as a protective layer (Fig. 7b–d), which shows a promising foreground in wearable protective clothing

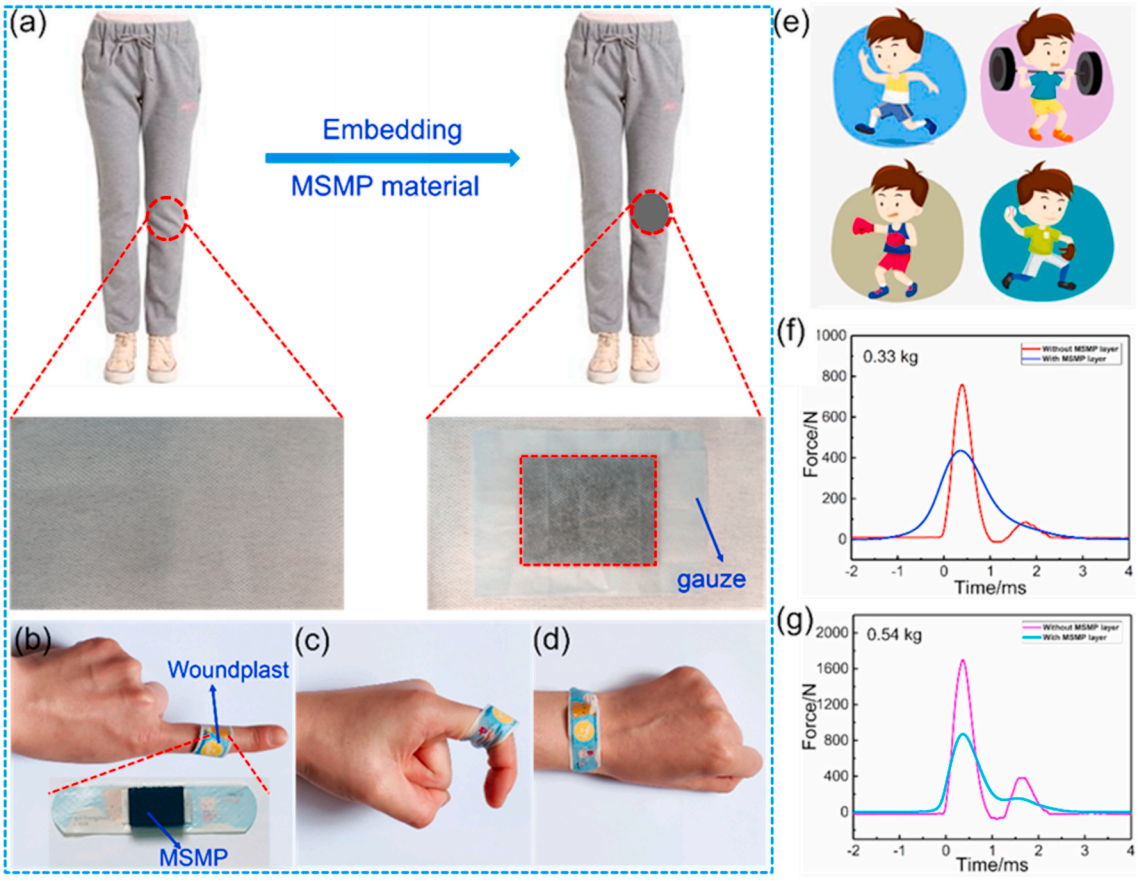

Fig. 7. The developed safety clothing for sports protective equipment by embedding $MSM_{57}P_{0.25}$ material into a common sportswear (a). The wearable protection property of as-prepared MSMP material which can be attached to different body parts, such as finger and wrist (b–d). Various sports that human beings often join to keep healthy or entertain, such as running, weightlifting, boxing and playing baseball (e). The force of sportswear with/without $MSM_{57}P_{0.25}$ material impacted by objects with 0.33 kg (f) and 0.54 kg (g) mass from 10 cm drop height.

fields. Finally, based on the flexibility, softness and light weight of $MSM_{57}P_{0.25}$ material, the obtained safety clothing as sports protective equipment could fit the human body well, providing protection and wearing comfort at the same time.

4. Conclusions

In this work, a flexible Melamine Sponge/MXene/Polyborosiloxane (MSMP) material is proposed by assembling conductive MXene and viscoelastic PBS into porous melamine sponge. The as-prepared MSMP material exhibits flexibility, light weight and easy processable molding advantages. Owing to the shear stiffening characteristic, MSMP material with safe-guarding and anti-impact performance can dissipate the external impact force from 810, 996, 1200, 1410 and 1550 N to 446, 716, 860, 1050 and 1250 N for 10, 15, 20, 25 and 30 cm drop height, respectively. More importantly, the MSMP material possesses outstanding EMI shielding performance and the maximum shielding value of $MSM_{57}P_{0.25}$ sample reaches to as high as 39 dB, which provides an effective protection for human beings under the electromagnetic radiation environment. Besides, due to the viscoelastic property and internal supramolecular network of polyborosiloxane, the as-prepared hybrid material reveals excellent adhesion ability at room temperature, endowing the material with a long lifetime. Finally, based on these multifunctional properties, a novel kind of lightweight protective clothing is developed by embedding MSMP material into the common sportswear as a liner, which can prevent collision damage and electromagnetic radiation injury, and protect sportsmen during the exercise. Therefore, this novel MSMP material shows wide application prospects in safe-guarding, wearable body protection equipment and EMI shielding fields, which caters to the development of multifunctional materials in the new era.

Author statement

Min Sang: Investigation, Writing - original draft, Methodology, Visualization.

Yuxuan Wu: Investigation, original draft, Formal analysis.

Shuai Liu: Investigation, original draft, Formal analysis.

Linfeng Bai: Formal analysis, Writing - review & editing, Data curation.

Sheng Wang: Investigation, Methodology, Data curation.

Wanquan Jiang: Investigation, Methodology, Data curation.

Shouhu Xuan: Form analysis, Methodology, Investigation, Writing - review & editing.

Xinglong Gong: Resources, Supervision, Project administration, Funding acquisition.

Declaration of competing interest

The authors declare that they have no known competing financial interests or personal relationships that could have appeared to influence the work reported in this paper.

Acknowledgements

Financial supports from the National Natural Science Foundation of

China (Grant Nos. 11822209, 12072338, 11772320), the Fundamental Research Funds for the Central Universities (WK2480000007) and Joint Fund of USTC-National Synchrotron Radiation Laboratory (KY2090000055) are gratefully acknowledged.

Appendix A. Supplementary data

Supplementary data to this article can be found online at https://doi.org/10.1016/j.compositesb.2021.108669.

References

[1] Liu M, Zhang S, Liu S, Cao S, Wang S, Bai L, Sang M, Xuan S, Jiang W, Gong X. CNT/STF/Kevlar-based wearable electronic textile with excellent anti-impact and sensing performance. Compos Part A-Appl S 2019;126:105612.

[2] Waitukaitis SR, Jaeger HM. Impact-activated solidification of dense suspensions via dynamic jamming fronts. Nature 2012;487:205–9.

[3] Kim Y, Sathish Kumar SK, Park Y, Kwon H, Kim CG. High-velocity impact onto a high-frictional fabric treated with adhesive spray coating and shear thickening fluid impregnation. Compos Part B-Eng 2020;185:107742.

[4] Cao S, Pang H, Zhao C, Xuan S, Gong X. The CNT/PSt-EA/Kevlar composite with excellent ballistic performance. Compos Part B-Eng 2020;185:107793.

[5] Bajya M, Majumdar A, Butola BS, Verma SK, Bhattacharjee D. Design strategy for optimising weight and ballistic performance of soft body armour reinforced with shear thickening fluid. Compos Part B-Eng 2020;183:107721.

[6] Liu B, Du C, Yu G, Fu Y. Shear thickening effect of a multifunctional magnetorheological gel: the influence of cross-linked bonds and solid particles. Smart Mater Struct 2020;29. 015004.

[7] Wang S, Ding L, Wang Y, Gong X. Multifunctional triboelectric nanogenerator towards impact energy harvesting and safeguards. Nano Energy 2019;59:434–42.

[8] Liu B, Du C, Jiang S, Zhou G, Sun J. The influence of the curing process on the shear thickening performance of RMG and property optimization. RSC Adv 2020;10(21):12197–205.

[9] Guo F, Du C-b, Yu G-j, Li R-p. The static and dynamic mechanical properties of magnetorheological silly putty. Ann Mater Sci Eng 2016;10:7079698.

[10] Boland CS, Khan U, Ryan G, Barwich S, Charifou R, Harvey A, Backes C, Li Z, Ferreira MS, Möbius ME, Young RJ, Coleman JN. Sensitive electromechanical sensors using viscoelastic graphene-polymer nanocomposites. Science 2016;354(6317):1257–60.

[11] Haro EE, Odeshi AG, Szpunar JA. The energy absorption behavior of hybrid composite laminates containing nano-fillers under ballistic impact. Int J Impact Eng 2016;96:11–22.

[12] Yuan F, Wang S, Zhang S, Wang Y, Xuan S, Gong X. A Flexible viscoelastic coupling cable with self-adapted electrical properties and anti-impact performance toward shapeable electronic devices. J Mater Chem C 2019;7(27):8412–22.

[13] Wang S, Gong L, Shang Z, Ding L, Yin G, Jiang W, Gong X, Xuan S. Novel safeguarding tactile e-skins for monitoring human motion based on SST/PDMS-AgNW-PET hybrid structures. Adv Funct Mater 2018;28(18):1707538.

[14] Yao B, Hong W, Chen T, Han Z, Xu X, Hu R, Hao J, Li C, Li H, Perini SE, Lanagan MT, Zhang S, Wang Q, Wang H. Highly stretchable polymer composite with strain-enhanced electromagnetic interference shielding effectiveness. Adv Mater 2020;14(32):1907499.

[15] Ma Z, Kang S, Ma J, Shao L, Zhang Y, Liu C, Wei A, Xiang X, Wei L, Gu J. Ultraflexible and mechanically strong double-layered aramid nanofiber–Ti3C2Tx MXene/silver nanowire nanocomposite papers for high-performance electromagnetic interference shielding. ACS Nano 2020;14:8368–82.

[16] Chen Y, Zhang HB, Yang YB, Wang M, Cao AY, Yu ZZ. High-performance epoxy nanocomposites reinforced with three-dimensional carbon nanotube sponge for electromagnetic interference shielding. Adv Funct Mater 2020;26(3):447–55.

[17] Gan W, Chen C, Giroux M, Zhong G, Goyal MM, Wang Y, Ping W, Song J, Xu S, He S, Jiao M, Wang C, Hu L. Conductive wood for high-performance structural electromagnetic interference shielding. Chem Mater 2020;32(12):5280–9.

[18] Yue Y, Liu N, Liu W, Li M, Ma Y, Luo C, Wang S, Rao J, Hu X, Su J, Zhang Z, Huang Q, Gao Y. 3D hybrid porous MXene-sponge network and its application in piezoresistive sensor. Nano Energy 2018;50:79–87.

[19] Seyedin S, Uzun S, Levitt A, Anasori B, Dion G, Gogotsi Y, Razal JM. MXene composite and coaxial fibers with high stretchability and conductivity for wearable strain sensing textiles. Adv Funct Mater 2020;30(12):1910504.

[20] Ma Y, Yue Y, Zhang H, Cheng F, Zhao W, Rao J, Luo S, Wang J, Jiang X, Liu Z, Liu N, Gao Y. 3D synergistical MXene/reduced graphene oxide aerogel for a piezoresistive sensor. ACS Nano 2018;12(4):3209–16.

[21] Lei Y, Zhao W, Zhang Y, Jiang Q, He JH, Baeumner AJ, Wolfbeis OS, Wang ZL, Salama KN, Alshareef HN. A MXene-based wearable biosensor system for high-performance in vitro perspiration analysis. Small 2019;15(19):1901190.

[22] Levitt A, Zhang J, Dion G, Gogotsi Y, Razal JM. MXene-based fibers, yarns, and fabrics for wearable energy storage devices. Adv Funct Mater 2020;30(47):2000739.

[23] Zhang X, Liu X, Yan R, Yang J, Liu Y, Dong S. Ion-assisted self-assembly of macroporous MXene films as supercapacitor electrodes. J Mater Chem C 2020;8(6):2008–13.

[24] Anasori B, Lukatskaya MR, Gogotsi Y. 2D metal carbides and nitrides (MXenes) for energy storage. Nat Rev Mater 2017;2:16098.

[25] Yu L, Fan Z, Shao Y, Tian Z, Sun J, Liu Z. Versatile N-doped MXene ink for printed electrochemical energy storage application. Adv Energy Mater 2019;9(34):1901839.

[26] Zhang Y, Wang L, Zhang J, Song P, Xiao Z, Liang C, Qiu H, Kong J, Gu J. Fabrication and investigation on the ultra-thin and flexible $Ti_3C_2T_x$/co-doped polyaniline electromagnetic interference shielding composite films. Compos Sci Technol 2019;183:107833.

[27] Song P, Qiu H, Wang L, Liu X, Zhang Y, Zhang J, Kong J, Gu J. Honeycomb structural rGO-MXene/epoxy nanocomposites for superior electromagnetic interference shielding performance. Sustain Mater Technol 2020;24:00153.

[28] Liu LX, Chen W, Zhang HB, Wang QW, Guan F, Yu ZZ. Flexible and multifunctional silk textiles with biomimetic leaf-like MXene/silver nanowire nanostructures for electromagnetic interference shielding, humidity monitoring, and self-derived hydrophobicity. Adv Funct Mater 2019;29(44):1905197.

[29] Jia X, Shen B, Zhang L, Zheng W. Waterproof MXene-decorated wood-pulp fabrics for high-efficiency electromagnetic interference shielding and Joule heating. Compo Part B-Eng 2020;198:108250.

[30] Chen W, Liu LX, Zhang HB, Yu ZZ. Flexible, transparent, and conductive $Ti_3C_2T_X$ MXene–silver nanowire films with smart acoustic sensitivity for high-performance electromagnetic interference shielding. ACS Nano 2020;14(12):16643–53.

[31] Wu X, Han B, Zhang H, Xie X, Tu T, Zhang Y, Dai Y, Yang R, Yu Z. Compressible, durable and conductive polydimethylsiloxane-coated MXene foams for high-performance electromagnetic interference shielding. Chem Eng J 2020;381:122622.

[32] Fan Z, Wang D, Yuan Y, Wang Y, Cheng Z, Liu Y, Xie Z. A lightweight and conductive MXene/graphene hybrid foam for superior electromagnetic interference shielding. Chem Eng J 2020;381:122696.

[33] Zhao S, Zhang H, Luo J, Wang Q, Xu B, Hong S, Yu Z. Highly electrically conductive three-dimensional $Ti_3C_2T_x$ MXene/reduced graphene oxide hybrid aerogels with excellent electromagnetic interference shielding performances. ACS Nano 2018;12:11193–202.

[34] Liang C, Qiu H, Song P, Shi X, Kong J, Gu J. Ultra-light MXene aerogel/wood-derived porous carbon composites with wall-like "mortar/brick" structures for electromagnetic interference shielding. Sci Bull 2020;65:616.

[35] Wang L, Qiu H, Song P, Zhang Y, Lu Y, Liang C, Kong J, Chen L, Gu J. 3D $Ti_3C_2T_x$ MXene/C hybrid foam/epoxy nanocomposites with superior electromagnetic interference shielding performances and robust mechanical properties. Compos Part A-Appl S 2019;126:105612.

[36] Hu T, Xuan S, Ding L, Gong X. Stretchable and magneto-sensitive strain sensor based on silver nanowire-polyurethane sponge enhanced magnetorheological elastomer. Mater Des 2018;156:528–37.

[37] Zhu S, Zhou Q, Wang M, Dale J, Qiang Z, Fan Y, Zhu M, Ye C. Modulating electromagnetic interference shielding performance of ultra-lightweight composite foams through shape memory function. Compos Part B-Eng 2021;204:108497.

[38] Zhussupbekova A, Caffrey D, Zhussupbekov K, Smith CM, Shvets IV, Fleischer K. Low-Cost, High-performance spray pyrolysis-grown amorphous zinc tin oxide: the challenge of a complex growth process. ACS Appl Mater Interfaces 2020;12(41):46892–9.

[39] Ma Z, Kang S, Ma J, Shao L, Wei A, Liang C, Gu J, Yang B, Dong D, Wei L, Ji Z. High-performance and rapid-response electrical heaters based on ultraflexible, heat-resistant, and mechanically strong aramid nanofiber/Ag nanowire nanocomposite papers. ACS Nano 2019;13:7578.

[40] Yang X, Fan S, Li Y, Guo Y, Li Y, Ruan K, Zhang S, Zhang J, Kong J, Gu J. Synchronously improved electromagnetic interference shielding and thermal conductivity for epoxy nanocomposites by constructing 3D copper nanowires/thermally annealed graphene aerogel framework. Compos Part A-Appl S 2020;128:105670.

[41] Wang S, Xuan S, Wang Y, Xu C, Mao Y, Liu M, Bai L, Jiang W, Gong X. Stretchable polyurethane sponge scaffold strengthened shear stiffening polymer and its enhanced safeguarding performance. ACS Appl Mater Interfaces 2016;8(7):4946–54.

[42] Zhang S, Wang S, Hu T, Xuan S, Jiang H, Gong X. Study the safeguarding performance of shear thickening gel by the mechanoluminescence method. Compos Part B-Eng 2020;180:107564.

[43] Wang Y, Gong X, Xuan S. Study of low-velocity impact response of sandwich panels with shear-thickening gel cores. Smart Mater Struct 2018;27. 065008.

[44] Zhao C, Xu C, Cao S, Xuan S, Jiang W, Gong X. Anti-impact behavior of a novel soft body armor based on shear thickening gel (STG) impregnated Kevlar fabrics. Smart Mater Struct 2019;28:075036.

[45] Hou K, Jin Y, Chen J, Wen X, Xu S, Cheng J, Pi P. Fabrication of superhydrophobic melamine sponges by thiol-ene click chemistry for oil removal. Mater Lett 2017;202:99–102.

[46] Chen J, You H, Xu L, Li T, Jiang X, Li CM. Facile synthesis of a two-tier hierarchical structured superhydrophobic-superoleophilic melamine sponge for rapid and efficient oil/water separation. J Colloid Interface Sci 2017;506:659–68.

[47] Zhang Y, Zhang Q, Zhang R, Liu S, Zhou Y. A superhydrophobic and elastic melamine sponge for oil/water separation. New J Chem 2019;43(16):6343–9.

[48] Tang M, Zheng P, Wang K, Qin Y, Jiang Y, Cheng Y, Li Z, Wu L. Autonomous adhesion, self-adhesive, highly conductive composites based on a silver-filled polyborosiloxane/polydimethylsiloxane double-network elastomer. J Mater Chem A 2019;7(48):27278–88.

[49] Rohith Vinod K, Saravanan P, Suresh Kumar TR, Radha R, Balasubramaniam M, Balakumar S. Enhanced shielding effectiveness in nanohybrids of graphene derivatives with Fe_3O_4 and ε-Fe_3N in the X-band microwave region. Nanoscale 2018;10(25):12018–34.

[50] Sang M, Wang S, Liu S, Liu M, Bai L, Jiang W, Xuan S, Gong X. A hydrophobic, self-powered, electromagnetic shielding PVDF-based wearable device for human body monitoring and protection. ACS Appl Mater Interfaces 2019;11(50):47340–9.
[51] Hu D, Huang X, Li S, Jiang P. Flexible and durable cellulose/MXene nanocomposite paper for efficient electromagnetic interference shielding. Compos Sci Technol 2020;188:107995.
[52] Cao M, Wang X, Zhang M, Shu J, Cao W, Yang H, Fang X, Yuan J. Electromagnetic response and energy conversion for functions and devices in low-dimensional materials. Adv Funct Mater 2019;29(25):1807398.
[53] Cao M, Wang X, Cao W, Fang X, Wen B, Yuan J. Thermally driven transport and relaxation switching self-powered electromagnetic energy conversion. Small 2018;14(29):1800987.
[54] Ramoa SDAS, Barra GMO, Merlini C, Livi S, Soares BG, Pegoretti A. Electromagnetic interference shielding effectiveness and microwave absorption properties of thermoplastic polyurethane/montmorillonite-polypyrrole nanocomposites. Polym Adv Technol 2018;29:1377–84.
[55] Jia X, Shen B, Zhang L, Zheng W. Construction of compressible Polymer/MXene composite foams for high-performance absorption-dominated electromagnetic shielding with ultra-low reflectivity. Carbon 2020;173:932–40.
[56] Chen Y, Wang Y, Zhang H, Li X, Gui C, Yu Z. Enhanced electromagnetic interference shielding efficiency of polystyrene/graphene composites with magnetic Fe_3O_4 nanoparticles. Carbon 2015;82:67–76.
[57] Pitkänen O, Tolvanen J, Szenti I, Kukovecz A, Hannu J, Jantunen H, Kordas K. Lightweight hierarchical carbon nanocomposites with highly efficient and tunable electromagnetic interference shielding properties. ACS Appl Mater Interfaces 2019;11(21):19331–8.
[58] Verma M, Verma P, Dhawan SK, Choudhary V. Tailored graphene based polyurethane composites for efficient electrostatic dissipation and electromagnetic interference shielding applications. RSC Adv 2015;5(118):97349–58.
[59] Jaiswal R, Agarwal K, Kumar R, Kumar R, Mukhopadhyay K, Prasad NE. EMI and microwave absorbing efficiency of polyaniline-functionalized reduced graphene oxide/c-Fe_2O_3/epoxy nanocomposite. Soft Matter 2020;16(28):6643–53.
[60] Hashemi SA, Mousavi SM, Arjmand M, Yan N, Sundararaj U. Electrified single-walled carbon nanotube/epoxy nanocomposite via vacuum shock technique: effect of alignment on electrical conductivity and electromagnetic interference shielding. Polym Compos 2018;39(S2):1139–48.